J Mater Sci (2015) 50:4047–4065
DOI 10.1007/s10853-015-8961-9

Non-coherent Cu grain boundaries driven by continuous vacancy loading

W. S. Yu[1] · M. J. Demkowicz[1]

Received: 26 November 2014 / Accepted: 9 March 2015 / Published online: 20 March 2015

Abstract We use atomistic modeling to study the response of three non-coherent grain boundaries (GBs) in Cu to continuous loading with vacancies. Our simulations yield insights into the structure and properties of these boundaries both near and far from thermal equilibrium. We find that GB energies vary periodically as a function of the number of vacancies introduced. Each GB has a characteristic minimum energy state that recurs during continuous vacancy loading, but in general cannot be reached without removing atoms from the boundary. There is no clear correlation of GB energies with GB specific excess volumes or stresses during vacancy loading. However, GB stresses increase monotonically with specific excess volumes. Continuous vacancy loading gives rise to GB migration and shearing, despite the absence of applied loads. Successive vacancies introduced into some of the boundaries accumulate at the cores of what appear to be generalized vacancy dislocation loops. We discuss the implications of these findings for our understanding of grain boundary sink efficiencies under light ion irradiation.

Motivation

Grain boundaries (GBs) are sinks for point defects, such as vacancies and interstitials [1–5]. This property of GBs may be used to improve the radiation resistance of polycrystalline solids [6–8]. Therefore, much effort has been invested into understanding the factors that determine the sink efficiency of GBs [9–12] as well as the effect of GB sinks on the properties of polycrystalline materials [9, 13, 14]. Less has been done to assess the impact of the absorption of point defects on the GBs themselves. However, there is ample experimental evidence to suggest that point defect absorption does impact GB structure and properties, especially when GBs are exposed to a continuous influx of point defects, as is the case under irradiation. For example, Han et al. [5] found that nanoscale cavities form on Cu GBs under light ion irradiation.

We present an atomistic modeling study of the response of three GBs in Cu to the continuous introduction of vacancies. All three of these GBs are coincidence site lattice (CSL) boundaries with low CSL numbers [15]. We nevertheless call them "non-coherent" because their plane inclinations give rise to large boundary unit cells and atomic-level structures that are less regular and more distorted than coherent boundaries (see Figs. 8, 9, 10). Our work shows that, under continuous vacancy loading, these GBs undergo a periodic variation in energy, structure, and properties. Moreover, continuous vacancy fluxes cause the GBs to migrate and shear, even though no external loads are applied. Our findings yield insights into the behavior of GBs both in and far from thermal equilibrium. They also advance our understanding of the connection between GB properties and the sink efficiency of GBs for absorbing vacancies.

Numerous atomistic modeling studies have been performed on GB interactions with point defects [16–20]. However, most treat isolated point defects interacting with GBs. For example, Suzuki et al. investigated binding of vacancies and self-interstitials at different Cu GB locations [21, 22] as well as their migration from one location to another within GBs [23]. Formation energies of isolated

✉ W. S. Yu
abinit@163.com

[1] Department of Materials Science and Engineering, Massachusetts Institute of Technology, Cambridge, MA 02139, USA

point defects at or near GBs have been calculated in several materials, such as W [16], Fe [16, 18, 20], Au [24], and MgO [25].

Fewer investigations have been devoted to the effect of adding numerous point defects to GBs. Early studies found that atomic-level GB structures undergo reconstructions as atoms are removed [26] and that a large number of non-equivalent structural configurations may be available to general, non-coherent boundaries [27]. Using a method for grand-canonical simulated quenching (GCSQ), Phillpot and Rickman found that GB energies may be reduced by removing atoms [28, 29]. Similarly, Von Alfthan and Sutton [30] showed that finding the lowest energy states of general GBs in Si often requires removing or adding atoms. Bai et al. studied loading of radiation-induced interstitials into Cu GBs and assessed its effect on recombination reactions with vacancies [31, 32]. In a study of two $\Sigma5\langle100\rangle$GBs in Cu interacting with reservoirs of atoms, Frolov et al. showed that GBs may undergo structural phase transitions [33]. Borovikov et al. investigated the effect of point defect loading on GB mobility in W [34]. All of these studies focused on a limited number of point defects being introduced into GBs. To create far-from-equilibrium GBs with high excess volume, Tucker and MacDowell [35] introduced a large number of vacancies at random locations in $\Sigma9\langle110\rangle$ and $\Sigma11\langle110\rangle$ tilt GBs in Cu and Al. However, the behavior of GBs in response to continuous influx of radiation-induced point defects has not been previously investigated.

The influx of vacancies into GBs and their subsequent diffusion within the GB plane occurs by thermally activated migration. Molecular dynamics (MD) may be used to simulate small numbers of such migration events at elevated temperatures [36–38]. However, the simulation times required to model a continuous vacancy influx by direct MD are prohibitively long, especially at low homologous temperatures. In some cases, vacancy diffusion to and within GBs may be modeled using kinetic Monte Carlo (kMC) methods [23, 39, 40]. These methods work best for GBs with relatively regular, ordered structures. However, we are interested in general, non-coherent GBs that may contain disordered regions.

To circumvent these modeling limitations, we do not attempt to simulate the kinetics of vacancy migration to and within GBs. Instead, we use a "quasi-static" vacancy loading algorithm where vacancies are introduced into GB sites with lowest vacancy formation energies. This approach is not intended to represent the true physical processes governing vacancy influx into GBs under irradiation. Instead, it constitutes an attempt at gauging the evolution of GB structure during continuous introduction of vacancies. In particular, we are interested in determining whether the introduction of vacancies into lowest energy positions leads to initiation of GB damage processes, such as formation of vacancy clusters that may constitute cavity or crack nuclei. Quasi-static introduction of vacancies into single crystals is known to initiate such damage processes [41, 42].

Although our quasi-static loading algorithm is not intended to represent any specific experimental condition, it may nevertheless be thought of as a limit where net vacancy fluxes are so small and vacancy mobility within GBs is so high that every vacancy arriving at a GB has enough time to diffuse through the boundary and find the lowest energy location for it to bind. Similar algorithms have been used to reduce GB and heterophase interface energies by removing or adding atoms [30, 43]. Indeed, our algorithm provides an effective way of finding low-energy GB structures, which approximate the thermal equilibrium state of well-relaxed boundaries at low temperature. Upon continued vacancy loading, this algorithm also drives GBs with initially low energies far from equilibrium, providing opportunities to study the physical properties of non-equilibrium GBs [35, 44–47].

In the "Atomic models of selected grain boundaries" section, we describe the construction of atomic models of the three non-coherent GB models chosen for this study. The "Continuous introduction of vacancies into grain boundaries" section details the algorithm we use to continuously load vacancies into these GB models. The "Area-average grain boundary response to continuous vacancy loading" section describes variations of area-average GB properties—namely energy, specific excess volume, and stress—in response to continuous vacancy loading. GB migration and shearing are also discussed. The "Atomic-level response of grain boundaries to vacancy loading" section describes variations in atomic-level GB structure during vacancy loading and how they relate to GB vacancy formation energies. Finally, the "Discussion" section discusses the implications of our study, particularly with respect to the connection between GB structure and sink efficiency for vacancy absorption.

Atomic models of selected grain boundaries

To facilitate comparisons of our simulations with experiments, we choose to model three specific non-coherent GBs that have been investigated experimentally. These boundaries are taken from work by Han et al. [5], who studied the response of sixteen Cu GBs to light ion irradiation at 723 K. They found that copious radiation-induced voids form far from the GBs and that there is a void denuded zone (VDZ) adjacent to each boundary. The width of this zone differs for each GB and is indicative of a boundary's ability to absorb vacancies, i.e., its vacancy

sink efficiency, η [15]. A wide VDZ indicates that the GB has high η, and a narrow VDZ indicates low η. We select three GBs with VDZ widths ranging from ~20 to ~55 nm.

Han et al. report the complete crystallographic character—misorientations as well as GB plane orientations—for all the GBs they studied. We have selected three of these boundaries for the current study. Their character is given in Table 1. Misorientation is specified through the rotation axis vector $\boldsymbol{\rho}$, expressed in the Grain A frame, and misorientation angle θ. The GB plane orientations are reported via their Miller index vectors $\bar{\boldsymbol{m}}_A$ and $\bar{\boldsymbol{m}}_B$, expressed in the coordinate systems of the two adjoining grains (grain A and B, respectively). To a good approximation, these directions satisfy $\hat{\boldsymbol{m}}_B \approx \boldsymbol{O}_j \boldsymbol{R} \hat{\boldsymbol{m}}_A$, where $\boldsymbol{R}$ is the misorientation rotation matrix derived from $\boldsymbol{\rho}$ and θ [15], $\bar{\boldsymbol{m}}_A$ and $\bar{\boldsymbol{m}}_B$ are unit vectors of $\bar{\boldsymbol{m}}_A$ and $\bar{\boldsymbol{m}}_B$, respectively, and $\boldsymbol{O}_j$ is a symmetry operation of the cubic lattice [48]. Table 1 also reports the nearest reciprocal coincidence site density Σ for each boundary [15, 49], the boundary VDZ width, and the index of the boundary in Table 1 in the work of Han et al. [5].

To avoid free surface effects in our simulations, we construct bilayer models of the three GBs in Table 1 with periodic boundary conditions (PBCs) imposed within the interface plane. The bilayers terminate with free surfaces in the direction perpendicular to the GB plane, as illustrated in Fig. 1. The free surfaces allow the neighboring crystals to adjust in that direction as vacancies are being loaded. Thus, no net stresses normal to the GB plane build up during our simulations. Since all three GBs of interest are CSL boundaries, PBCs may be imposed without straining or rotating either of the adjacent crystals.

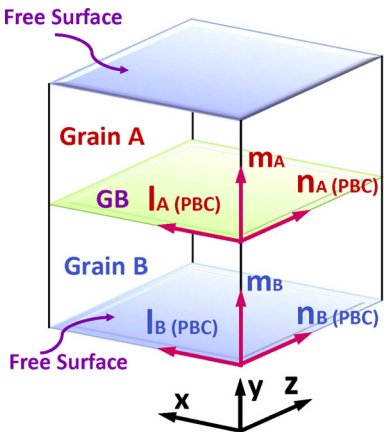

Fig. 1 Schematic of GB models

Our models are intended to represent GBs between stress-free, semi-infinite crystals. However, because our models are finite, the surface and GB stresses in them give rise to small, but non-zero distortions in the crystalline grains, if the simulation cell shape is allowed to relax. These distortions vanish in the limit of semi-infinite crystal grains (the limit we are trying to represent) because the ratio of GB and surface area to the volume of the bicrystal goes to zero in that limit. To represent this limit in finite-size models, the shape of the neighboring crystals parallel to the GB plane is held fixed at the shape corresponding to zero-stress perfect crystals.

Table 1 Crystallographic, physical, and modeling parameters for the three Cu GBs investigated in the present work

Grain boundaries (GB)[a]	Σ	Σ9	Σ11	Σ3
GB index in Table 1 of Ref. [5][a]	#	6	12	15
Misorientation angle (deg)[a]	θ	38.8	51.5	60
Rotation axis[a]	$\boldsymbol{\rho}$	$[01\bar{1}]$	$[21, \bar{1}, \bar{1}9]$	$[\bar{1}11]$
GB planes[a]	$\bar{\boldsymbol{m}}_A$	$[26, \bar{2}, 11]_A$	$[9, \bar{7}, \bar{1}9]_A$	$[14, \bar{1}\bar{7}, 17]_A$
	$\bar{\boldsymbol{m}}_B$	$[\bar{9}, 15, 1]_B$	$[\bar{2}\bar{8}, \bar{2}, \bar{1}\bar{1}]_B$	$[4, \bar{2}\bar{4}, 7]_B$
VDZ width (nm)[a]	λ	39	53 ± 14	22 ± 2
Crystalline orientations of Grain A	$\boldsymbol{l}_A$	$[11\bar{2}]$	$[1\bar{1}1]$	[110]
	$\boldsymbol{m}_A$	[201]	$[1\bar{1}\bar{2}]$	$[1\bar{1}1]$
	$\boldsymbol{n}_A$	$[1\bar{5}\bar{2}]$	[110]	$[1\bar{1}\bar{2}]$
Crystalline orientations of Grain B	$\boldsymbol{l}_B$	$[12\bar{7}]$	$[1, \bar{1}9, 1]$	$[01\bar{1}]$
	$\boldsymbol{m}_B$	$[2\bar{1}0]$	$[7, \bar{1}, \bar{2}6]$	[511]
	$\boldsymbol{n}_B$	$[\bar{7}, \bar{1}\bar{4}, 5]$	[15, 1, 4]	$[2\bar{5}\bar{5}]$
Dimension of model (Å)	x	53.1	68.8	20.4
	y	80.0	100.0	100.0
	z	59.4	56.2	53.1
Tilt axis/angle (deg)		⟨221⟩/180	⟨421⟩/155.4	⟨110⟩/70.5
Twist axis/angle (deg)		/	$[7, \bar{1}, \bar{2}6]$/40.3	/

[a] Taken from Ref [5]

The model sizes required to reproduce the high-index GB planes $\bar{\boldsymbol{m}}_{\mathrm{A}}$ and $\bar{\boldsymbol{m}}_{\mathrm{B}}$ listed in Table 1 are too large for our purposes. Therefore, we construct models of manageable size with lower index GB planes, described by unit normal vectors $\bar{\boldsymbol{m}}_{\mathrm{A}}$ and $\bar{\boldsymbol{m}}_{\mathrm{B}}$, that approximate $\bar{\boldsymbol{m}}_{\mathrm{A}}$ and $\bar{\boldsymbol{m}}_{\mathrm{B}}$. These lower index GB planes are given in Table 1 and are always within 6° of the experimentally determined ones.

As a result of this approximation, our models may have higher atom coincidence in the GB plane than the GBs in Ref. [5]—i.e., a smaller GB unit cell—which in turn may lead to lower GB energy [50]. The spacing between any intrinsic GB defects, such as misfit dislocations [15, 51], may also be different in our models than in the experiments. However, none of the GBs studied here are formed by joining two minimal-index or closest-packed crystallographic planes, such as {100}, {110}, or {111}, so none of them exhibit a high degree of coherency. A description of the atomic-level structure of these boundaries is presented in the "Structures of minimum energy GB states" section.

To construct atomic GB models, we define orthogonal directions $\boldsymbol{l}_{\mathrm{A}}$ and $\boldsymbol{n}_{\mathrm{A}}$ within the GB plane of grain A. $\boldsymbol{l}_{\mathrm{A}}$ and $\boldsymbol{n}_{\mathrm{A}}$ are also orthogonal to $\bar{\boldsymbol{m}}_{\mathrm{A}}$. By operating on $\boldsymbol{l}_{\mathrm{A}}$, $\bar{\boldsymbol{m}}_{\mathrm{A}}$, and $\boldsymbol{n}_{\mathrm{A}}$ with the misorientation rotation matrix $\boldsymbol{R}$, we obtain the corresponding directions for grain B: $\boldsymbol{l}_{\mathrm{B}}$, $\bar{\boldsymbol{m}}_{\mathrm{B}}$, and $\boldsymbol{n}_{\mathrm{B}}$. All of these directions are given in Table 1 for all three GBs. Two grains with the specified crystalline orientations are created by arranging atoms into layers with the dimensions shown in Table 1. A bicrystal is then created by joining the two grains. The first GB listed in Table 1 is a Σ9 symmetric tilt GB with crystallographically equivalent GB planes $[201]_A//[2\bar{1}0]_B$ and tilt axis/angle $[1\bar{2}\bar{2}]/180°$. The second is a Σ11 GB of mixed tilt/twist character with components of tilt axis/angle [421]/155.4° and twist axis/angle $[7, \bar{1}, 2\bar{6}]/40.3°$ obtained using the procedure in Ref. [48]. The last is a Σ3 asymmetric tilt GB (ATGB) with ⟨110⟩ tilt axis and inclination angle of 70.53° with respect to coherent Σ3 twin boundary, as investigated by Tschopp et al. [52].

We use the embedded atom method (EAM) [53] potential for Cu developed by Mishin et al. [54] to describe interatomic bonding in our GBs. To relax our models, we compute their γ surfaces and relax each structure using conjugate gradient (CG) energy minimization [55] starting from the relative position with lowest γ value. These configurations are then annealed for 100 ps at 700 K in the NVT ensemble using molecular dynamics (MD) with a Nosé–Hoover thermostat [56, 57]. Finally, the energies of the annealed structures are once again minimized using the CG method. The energies of all three GBs at different stages of relaxation are reported in the "Area-average grain boundary response to continuous vacancy loading" section.

All simulations are performed using LAMMPS [58]. Visualizations are performed in Ovito [59].

Continuous introduction of vacancies into grain boundaries

The absence of voids in a zone adjacent to the GBs in Han et al.'s study [5] as well as the presence of nanoscale voids within the GBs themselves implies that there is a net flux of vacancies into the boundaries. To investigate the effect of a continuous vacancy influx into GBs on GB structure evolution, we use a two-step, iterative algorithm. In the first step, we determine vacancy formation energies at all locations within a 16 Å-thick slab centered on the GB. As will be shown in the "GB vacancy formation energies" section, this thickness is sufficient to include all GB sites with vacancy formation energies markedly different from those in fcc Cu. A vacancy is created by deleting an atom and relaxing the model using the CG method. The vacancy formation energy E_{v} is computed as $E_{\mathrm{v}} = E^{\mathrm{Total}}_{\mathrm{GB,v}} - E^{\mathrm{Total}}_{\mathrm{GB}} - E^{\mathrm{Coh}}$, where $E^{\mathrm{Total}}_{\mathrm{GB,v}}$ and $E^{\mathrm{Total}}_{\mathrm{GB}}$ are the total energies of the GB model with and without the vacancy. E^{Coh} $(= 3.54\ \mathrm{eV})$ is the cohesive energy per atom of fcc Cu [54]. In the second step, we create a new GB structure by introducing a vacancy at the location of lowest formation energy $E^{\mathrm{min}}_{\mathrm{v}}$. These two steps are then repeated using the new GB structure as the starting configuration.

By repeating the steps described above hundreds of times for each of the GB models described in the "Atomic models of selected grain boundaries" section, we obtain insight into how the structure and properties of these boundaries change with continuous vacancy loading. Although our algorithm does not correspond directly to any real, physical process, it may be viewed as analogous to vacancies diffusing from a crystal into the GB at a rate sufficiently low that each vacancy reaches its lowest energy location within the GB before the next vacancy arrives. Similar algorithms have been used to find low energy states of GBs and heterophase interfaces by removing or adding atoms [30, 43].

Area-average grain boundary response to continuous vacancy loading

As vacancies are loaded into the GB models described in the "Atomic models of selected grain boundaries" section, area-average properties such as GB energy, specific excess volume, and GB stresses change. Additionally, the GBs migrate (i.e., displace perpendicular to the GB plane) and

shear (the neighboring grains undergo a relative displacement parallel to the GB plane). These responses to vacancy loading are described below.

Grain boundary energies

To compute GB energy, we evaluate the atomic EAM energy [60] of all atoms i, E_i, within a region that includes the GB and terminates a distance $2r_{cut}$ away from top and bottom free surfaces, where r_{cut} is the cutoff radius of the potential. This way, the free surfaces are excluded from the calculation. GB energy is then computed as

$$\gamma_{GB} = \frac{\sum_i \left(E_i - E^{Coh}\right)}{A_{GB}}, \quad (1)$$

where A_{GB} is the GB area.

For the three GBs studied here, Fig. 2a–c plots γ_{GB} as a function of the number of vacancies loaded, n, as well as number of vacancies loaded per unit GB area, n/A_{GB}. Three values are shown at $n = 0$: the first one is for the as-constructed GB before the MD anneal (triangle) and the second for the GB after a 100 ps 700 K MD anneal (diamond). We also plotted a third value: one obtained for a GB relaxed by melting followed by slow recrystallization (circle). To obtain the latter GB energy, the region near the GB is heated until it melts and then slowly cooled, allowing the GB region to recrystallize.

For the Σ9 and Σ11 GBs, we also obtained a fourth value using the method of Tschopp et al. [52, 61, 62], which relaxes GB structures using energy minimization starting from different initial relative translations of the neighboring crystals. Atoms are removed from the unrelaxed GB models if they are closer together than a prespecified cutoff distance (between 0.275 and 0.7 a, where a is the cubic lattice parameter). We sampled relative displacements on a 5 × 5 grid covering one unit cell of the GB γ surfaces and tried five different atom deletion cutoff distances, within the range suggested by Tschopp et al. [52, 61, 62]. The values plotted in Fig. 2a and b are the lowest GB energies obtained using this method.

For Σ9 and Σ11 GBs, the MD anneal, GB-recrystallization, and the method of Tschopp et al. all reduce the GB energy, compared to the as-constructed state. For the Σ3 GB, the MD anneal has no effect on the GB energy. However, recrystallization of the Σ3 GB leads to a higher GB energy because the GB dissociates into two separate boundaries during the liquid–solid phase transformation. As vacancies are loaded, γ_{GB} initially decreases for the Σ9 and Σ11 GBs and increases for the Σ3. Upon continued vacancy loading, γ_{GB} for the Σ9 and Σ11 GBs reaches minima. The minimum energy Σ9 GB generated has lower energy than that obtained using the method of Tschopp et al., while the minimum energy Σ11 GB has the same energy as that made using the method of Tschopp et al. By contrast, the Σ3 GB is close to a minimum γ_{GB} state at $n = 0$. In agreement with Ref. [52], we find $\gamma_{GB}(0) = 0.628\ \mathrm{Jm}^{-2}$ for the Σ3 GB. There have been no previous studies on Σ9 and Σ11 GBs with the specific GB planes investigated here, so there are no precedents against which to compare our findings.

As vacancies are loaded past the first minimum energy GB state, γ_{GB} varies periodically for all three GBs. The shapes of the $\gamma_{GB}(n)$ curves are qualitatively similar for all three GBs: each GB has characteristic minimum and maximum energies that recur at regular intervals of vacancy loading. Between energy minima, $\gamma_{GB}(n)$ has an approximately parabolic shape. γ_{GB} varies smoothly, except near the energy minimum, where it appears to have a cusp, i.e., a discontinuity in its first derivative. The GB states at the cusps of these energy curves are local energy minima. There is no guarantee that any of them is the global energy minimum for a given GB.

The as-annealed Σ3 GB is close to its minimum energy state. However, both the Σ9 and Σ11 GBs are far from their minimum energies after the MD anneal as well as after melting and recrystallization. Moreover, the energies of the annealed and recrystallized Σ11 GB are higher than the maximum energy that recurs in this boundary upon continuous vacancy loading. These findings are consistent with the view that, in general, the minimum energy state of an atomic GB model cannot be reached by annealing alone, but rather requires addition or removal of atoms [15, 30].

Energy minima, maxima, and periods for all three GBs are given in Table 2. The ranges of γ_{GB} for the three GBs are around 0.049, 0.009, and 0.123 Jm^{-2}, comparable to the variation range of GB energies for Cu Σ5 GBs at various states [33]. GB energy minima and maxima in Table 2 are also comparable to energies of GBs with different GB planes for Σ9 [63], Σ11 [63, 64], and Σ3 [52] misorientations, modeled with the same EAM potential for Cu as the one used here. For each of the three GBs, Table 2 also lists the areal densities of atoms in the two crystallographic planes that meet at the boundary. We find that the number of vacancies per unit area n^T/A_{GB} loaded into a GB during one period of its energy plot is very nearly equal to the average of the areal density of atoms of the crystallographic planes n^A/A_{GB} and n^B/A_{GB} that meet at the boundary, which we term $\bar{\rho}$.

Grain boundary specific excess volumes

We compute GB specific excess volumes, Δv_{GB}, from the Voronoi volumes Ω_i—calculated using Voro++ [65]—of all atoms within a slab of thickness 16 Å centered on the

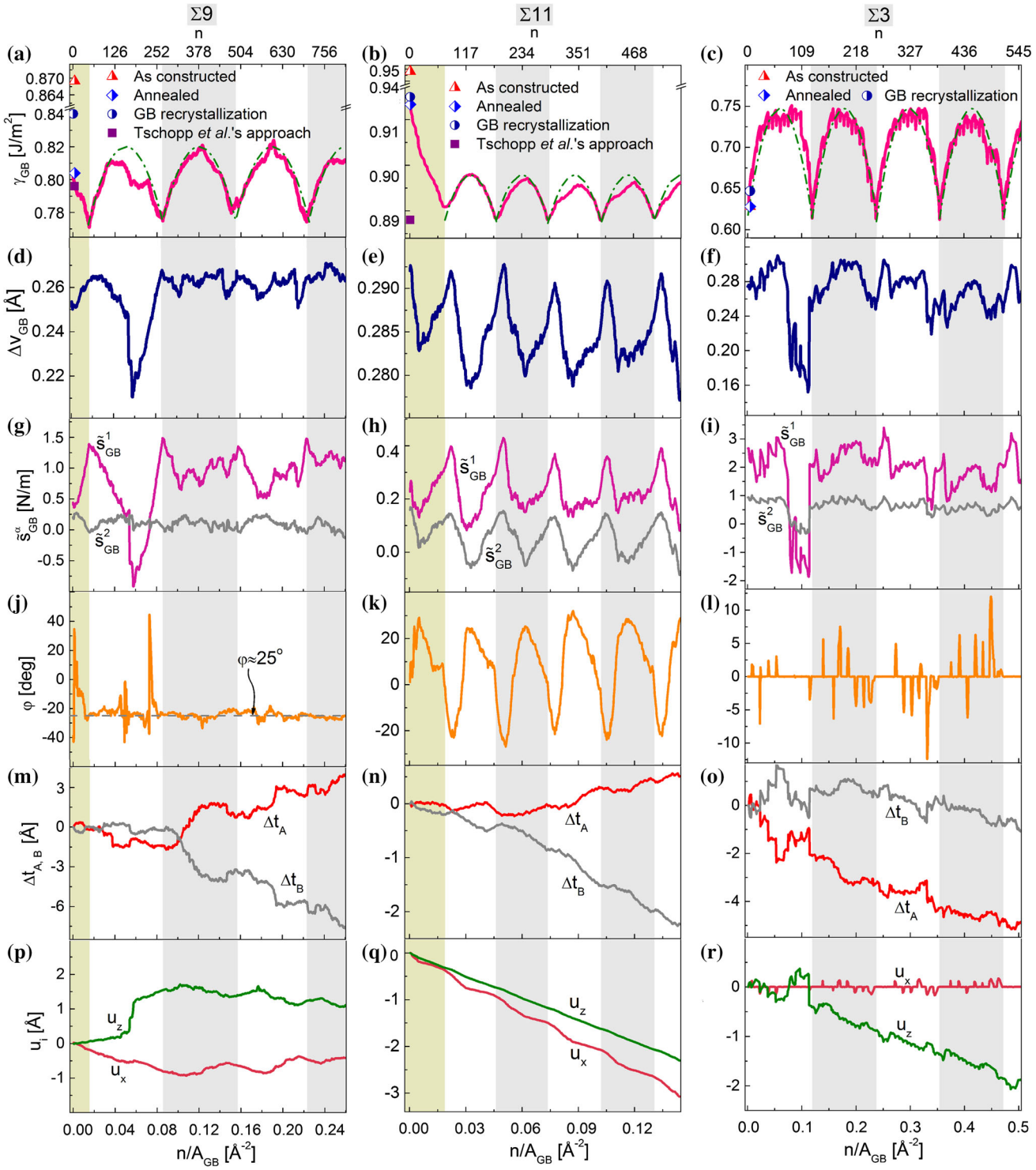

Fig. 2 Area-average properties of the Σ9 (*left column*), Σ11 (*middle column*), and Σ3 (*right column*) GBs as functions of the number of vacancies loaded, n, as well as the number of vacancies loaded per unit GB area, n/A_{GB} **a–c** GB energies γ_{GB}, the *triangle* and *diamond* in **c** have identical *values* and overlap; **d–f** specific GB volume Δv_{GB}; **g–i** principal GB stresses s^{ij}_{GB}; **j–l** orientation of the GB stress principal coordinate system φ; **m–o** changes in grain thickness Δt_A and Δt_B relative to the initial thickness; and **p–r** relative displacements u_x and u_z between the grains parallel to the GB plane

Table 2 Quantities characterizing variations of GB energy with vacancy loading, shown in Fig. 2a–c

		Σ9	Σ11	Σ3
Atom areal density in the terminal planes of grain A and B [Å^{-2}]	n^{A}/A_{GB}	0.068	0.062	0.176
	n^{B}/A_{GB}	0.068	0.006	0.059
Average atom areal density in the GB terminal planes [Å^{-2}]	$\bar{\rho}$	0.068	0.034	0.118
Periodicity of GB energy variation with vacancy loading [Å^{-2}]	n^{T}/A_{GB}	0.069	0.027	0.120
GB energy maxima and minima [Jm^{-2}]	γ_{GB}^{Max}	0.824	0.897	0.751
	γ_{GB}^{Min}	0.775	0.888	0.628

GB. This slab is sufficiently thick to include all atoms whose Ω_i deviates markedly from the zero temperature atomic volume of fcc Cu, $\Omega = 11.81$ Å^3. Δv_{GB} is the difference between Ω_i and Ω summed over all atoms in the slab and divided by the GB area:

$$\Delta v_{GB} = \frac{\sum_i (\Omega_i - \Omega)}{A_{GB}}. \quad (2)$$

Figure 2d–f plots Δv_{GB} as a function of n as well as n/A_{GB}. All Δv_{GB} fall within the range 0.15–0.3 Å, in qualitative agreement with previous studies on Cu ⟨001⟩ symmetrical tilt grain boundaries (STGBs) and (221)(001) asymmetrical twist boundaries [66]. Figure 2e shows regular, periodic variations in Δv_{GB} for the Σ11 GB. However, no clear trend in the variations of Δv_{GB} can be discerned for the Σ9 or the Σ3 GBs in Fig. 2d and f.

Grain boundary stresses

Much like free surfaces, GBs exert stresses on the adjoining crystalline grains [67–69]. We compute the components of the GB stress tensor as

$$s_{GB}^{ij} = \frac{\sum_m \sigma_m^{ij} \Omega_m}{A_{GB}}, \quad (3)$$

where σ_m^{ij} is the ijth component of the atomic virial stress tensor. The sum is taken over all atoms in the same region as that used to compute GB energy, so free surfaces do not contribute to s_{GB}^{ij}. We construct our GB models such that the stresses far from the GB are zero in both grains, so s_{GB}^{ij} reflects only GB stresses. Because the GBs in our models are planar, the only non-zero components of s_{GB}^{ij} are s_{GB}^{xx}, s_{GB}^{zz} , and s_{GB}^{xz}. From these values, we obtain the principal GB stresses $\tilde{s}_{GB}^{\alpha}$ of s_{GB}^{ij} as well as the orientation of the principal coordinate system, expressed as the angle φ between the x axis (see Fig. 1) and the eigenvector corresponding to principal stress s_{GB}^{α}.

Figure 2g–i shows the dependence of the principal GB stresses on the number of vacancies loaded. The values of these stresses range between −2.0 and 3.0 Nm^{-1}. We are not aware of any previous reports of GB stresses in Cu. However, the GB stresses we calculated are of the same order of magnitude as those reported for other transition metals, namely Ag, Fe, and Pd [70, 71]. As in the case of Δv_{GB}, no clear trends for GB stress variations are apparent in the Σ9 and Σ3 GBs, while for the Σ11 GB, $\tilde{s}_{GB}^{1}$ and $\tilde{s}_{GB}^{2}$ vary periodically, as shown in Fig. 2h. Figure 2j–l displays variations ofφ versus n. Aside from what appear to be isolated fluctuations, φ remains near 0° and −25° for the Σ3 and Σ9 GBs, respectively: the principal coordinate systems are invariant with respect to vacancy loading in these GBs. By contrast, the principal coordinate system for the Σ11 GB varies periodically with n, as depicted in Fig. 2k.

Grain boundary migration and shearing

Our study reveals that the continuous introduction of vacancies causes GBs to migrate and to shear, even though no external mechanical loads are applied. To characterize migration, we calculate how the thicknesses, t_A and t_B, of the neighboring grains change as vacancies are loaded into GBs. GB migration is said to occur if one grain becomes thicker, while the other becomes thinner. t_A and t_B are computed as differences between the y-coordinate of the GB, $\bar{y}_{GB}$, and the y-coordinates of the free surfaces of grains A and B $\bar{y}_{Surf}^{A}$, $\bar{y}_{Surf}^{B}$. These quantities—$\bar{y}_{GB}$, $\bar{y}_{Surf}^{A}$, and $\bar{y}_{Surf}^{B}$—are evaluated by averaging the y-coordinates of all atoms in the GB and two free surfaces. Atoms whose centro-symmetry parameters are greater than 0.5 are treated as part of the GB and the free surfaces [72].

To characterize GB shearing, we compute the relative displacements u_x and u_z between the grains parallel to the GB plane. u_x and u_z are obtained by comparing the positions of atoms on the top and bottom surfaces of GB model. GB shearing occurs if u_x or u_z changes monotonically while there is no GB migration. Changes in u_x or u_z occurring concurrently with GB migration may indicate that the GB is undergoing shear-coupled migration [73].

Figure 2m–o shows changes in grain thickness Δt_A and Δt_B (relative to the initial thickness), while Fig. 2p–r shows relative displacements u_x or u_z for all three GBs studied here. For the first ∼250 vacancies loaded into the Σ9 GB, u_x and

u_z change while Δt_A and Δt_B remain constant, indicating GB shearing. For n greater than ~ 250, u_x and u_z remain approximately constant while Δt_A increases and Δt_B decreases, consistent with non-shear-coupled GB migration. The Σ3 GB exhibits the reverse sequence of events: non-shear-coupled GB migration up to a vacancy loading of ~ 100 and GB shearing afterward. These results show that, under continuous vacancy loading, GBs may switch from migration to shearing and vice versa. For the Σ3 GB, both for $n > \sim 100\Delta t_A$ and Δt_B decrease monotonically at nearly identical rates, suggesting no GB migration. However, a monotonic decrease in u_z indicates that the GB is shearing.

The behavior of the Σ11 GB is distinct from the Σ9 and Σ3. It exhibits a monotonic decrease in Δt_B, a slight increase in Δt_A, as well as simultaneous monotonic changes in both u_x and u_z. These variations suggest that the GB is migrating and that part of this migration may be shear-coupled. To estimate the coupling factors, we first use least squares fitting to find the best-fit linear equations relating n to the GB migration distance, $\Delta y_{GB} = \Delta t_A - \Delta t_B$, and to the shearing displacements, u_x and u_z: $\Delta y_{GB} = 0.0051n - 0.4339$, $u_x = -0.0052n - 0.0539$, and $u_z = -0.0040n - 0.0254$. From these fits, we find coupling factors $u_x'/\Delta y_{GB}' = -1.02$ and $u_x'/\Delta y_{GB}' = -0.78$.

However, because the Σ11 GB is of mixed tilt/twist character, it seems unlikely that the observed shearing is due entirely to shear-coupled migration. If the GBs were to migrate with no additional in-plane GB shearing, then it would be expected to generate a twist as well as a shear. The PBCs applied in our model, however, do not allow for any relative twist between the neighboring grains. Therefore, if shear-coupled migration of the Σ11 GB were indeed occurring, then some additional mechanism—such as in-plane GB shearing—would still be required to accommodate the no-twist constraint arising from PBCs.

Correlations among area-average GB properties

In addition to characteristic dependencies on n, the GB properties discussed above may also be correlated to each other. For example, several authors have suggested that high GB specific excess volumes are correlated with high GB energies [66, 74–81]. Figure 3 plots γ_{GB} of all GB structures investigated here against their Δv_{GB} values. We find that minimum GB energies—indicated by diamond symbols in Fig. 3—increase monotonically with specific excess volume. However, when all the GB energies and specific excess volume are taken into account, no clear correlation is observed. Even in the Σ11 GB, where both γ_{GB} and Δv_{GB} exhibit periodic variations with n, these two quantities are not correlated with each other. Thus, the relationship between γ_{GB} and Δv_{GB} discussed in Ref. [66, 74–81] should be understood to apply to comparisons between different GBs in their minimum energy states, not to comparisons between different states of the same GB or between different GBs driven far from equilibrium. Figure 3 also shows that the GBs that exhibit large fluctuations in γ_{GB} upon continuous vacancy loading also exhibit large fluctuations in Δv_{GB}. Moreover, GBs with large γ_{GB} fluctuations tend to have lower average GB energies.

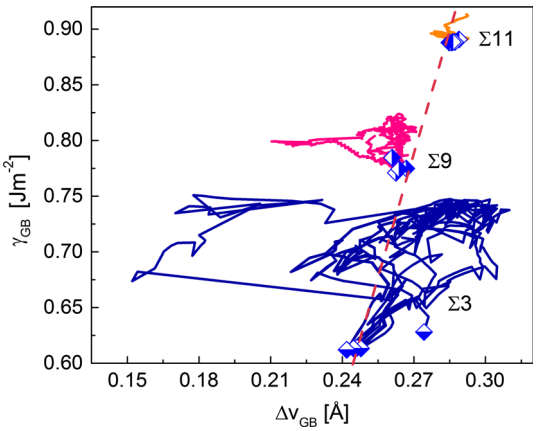

Fig. 3 GB energy γ_{GB} plotted as a function of GB specific excess volume Δv_{GB} for all structures investigated in this study. *Diamonds* show GBs in their minimum energy states. The *dashed line* illustrates the monotonic relationship between Δv_{GB} and γ_{GB} for GBs in minimum energy states

Figure 4 plots GB stresses $\tilde{s}_{GB}^1$ and $\tilde{s}_{GB}^2$ against Δv_{GB} for all three GBs, showing that $\tilde{s}_{GB}^{\alpha}$ increases monotonically with Δv_{GB}. $\tilde{s}_{GB}^1$ and $\tilde{s}_{GB}^2$ increase with Δv_{GB} in all cases except $\tilde{s}_{GB}^2$ in the Σ9 GB, which is nearly zero regardless of Δv_{GB}. These findings agree with the view of Birringer and Zimmer, who proposed that GB stresses may be thought of as arising from an effective "misfit" between the GB and the neighboring grains due to the excess specific volume of the former [70]. GB stresses are not correlated to GB energies. This is to be expected since GB specific excess volumes are not correlated to GB energies and GB stresses are correlated to GB specific excess volumes.

Finally, there appears to be a qualitative relationship between Δv_{GB} and GB shearing and migration in the Σ9 and Σ3 GBs. There is a switch from GB shearing to GB migration or vice versa at $n \approx 250$ and $n \approx 100$ in the Σ9 and Σ3 GBs, respectively. In both GBs, this switch is preceded by a gradual reduction in Δv_{GB} and is coincident with a rapid rise in Δv_{GB} as shown in Fig. 2d and f. Similar variations in $\tilde{s}_{GB}^1$ may be seen, as displayed in Fig. 2g and i. These sudden changes of Δv_{GB} and $\tilde{s}_{GB}^{\alpha}$ correspond to the variation range in Fig. 4a and c when $\Delta v_{GB} < 0.24$ and 0.23 Å for Σ9 and Σ3 GBs. Thus, switches between migration and shearing may be due to a gradual buildup of structural changes in the GB that relax rapidly once some critical condition is reached.

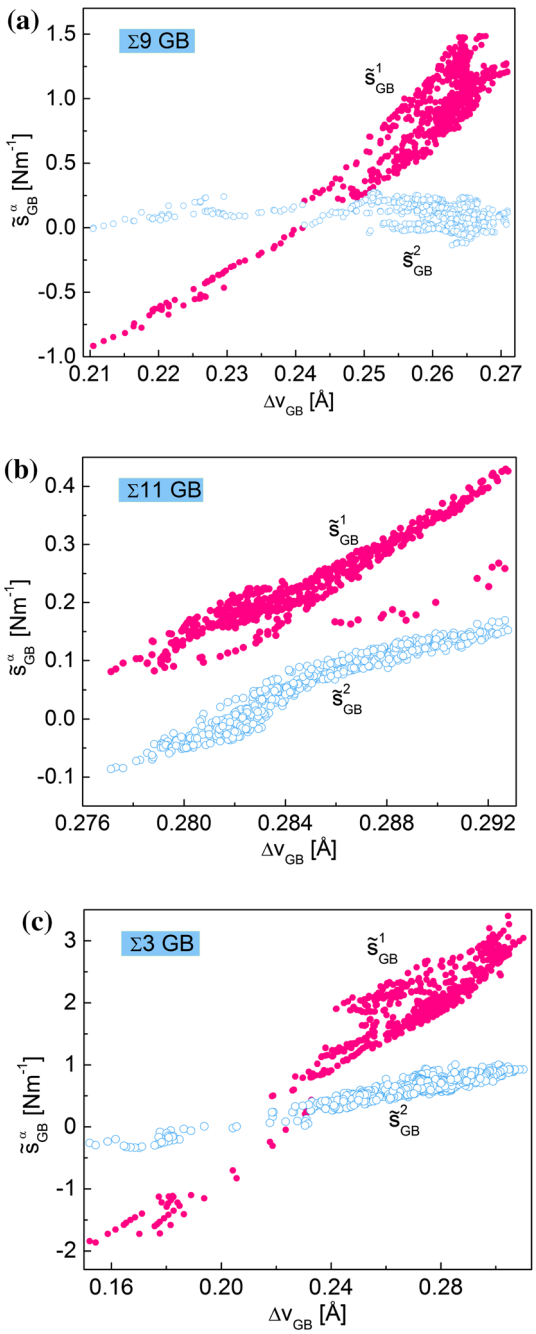

Fig. 4 GB stresses $\tilde{s}^1_{GB}$ and $\tilde{s}^2_{GB}$ plotted as functions of GB specific excess volume Δv_{GB} for the **a** Σ9, **b** Σ11, and **c** Σ3 GB

Atomic-level response of grain boundaries to vacancy loading

The structure of the GBs studied here changes as vacancies are loaded into them. While the previous five sections discussed area-averaged properties of GBs, the following three sections describe atomic-level structures of the GBs under investigation, focusing on the distributions of vacancy formation energies near the GBs and stresses normal to the GB planes.

GB vacancy formation energies

As shown in the "Grain boundary energies" section, all three of the GBs investigated here reach minimum energy states upon loading with vacancies. For the Σ3 GB, the first minimum energy state occurs at $n = 0$, i.e., in the as-constructed boundary. However, for the Σ9 and Σ11 GBs, the first minimum energy states occur at $n = 49$ and $n = 75$, respectively. The as-constructed, annealed, and recrystallized Σ9 and Σ11 GBs are not in lowest energy states. The spectrum of vacancy formation energies found in a given GB depends on whether or not the boundary is in its lowest energy state.

Figure 5 plots vacancy formation energies as a function of distance from the GB plane for the as-constructed and annealed states of the Σ9 and Σ11 boundaries. A wide distribution of vacancy formation energies is found in all cases, ranging from slightly above the vacancy formation energy in fcc Cu (1.27 eV, for the EAM potential used here [54]) down to negative values. When the formation energy of a GB vacancy is negative, this indicates that creating the vacancy reduces the GB energy. Annealing reduces the number of negative vacancy formation energy sites, but does not remove them all. Furthermore, the minimum vacancy formation energies are lower in the annealed GB structures than in the as-constructed ones.

Figure 6 shows vacancy formation energies as a function of distance from the GB plane at the first minimum energy structure found for each GB. As in Fig. 5, each GB exhibits a range of vacancy formation energies with maximum values exceeding the vacancy formation energy in fcc Cu. However, unlike in Fig. 5, Fig 6 shows no negative vacancy formation energy sites in any of the GBs. Thus, removing a vacancy from any of these structures causes the GB energy to increase. Indeed, none of the minimum energy GB states simulated here contain any negative vacancy formation energy sites. By contract, GBs that are not in a minimum energy state in general do contain negative vacancy formation energy sites.

In both Figs. 5 and 6, all the vacancy sites with formation energies markedly different from that of fcc Cu fit within a zone of width 16 Å centered on the GB. Therefore, our strategy of searching for lowest vacancy formation energy sites within this zone (described in the "Continuous introduction of vacancies into grain boundaries" section) is justified.

Figure 7 plots the dependence of minimum vacancy formation energy as a function of number of vacancies loaded for all three GBs studied here. All minimum energy states for any given GB have nearly identical minimum vacancy formation energies: ~0.46 eV for the Σ9,

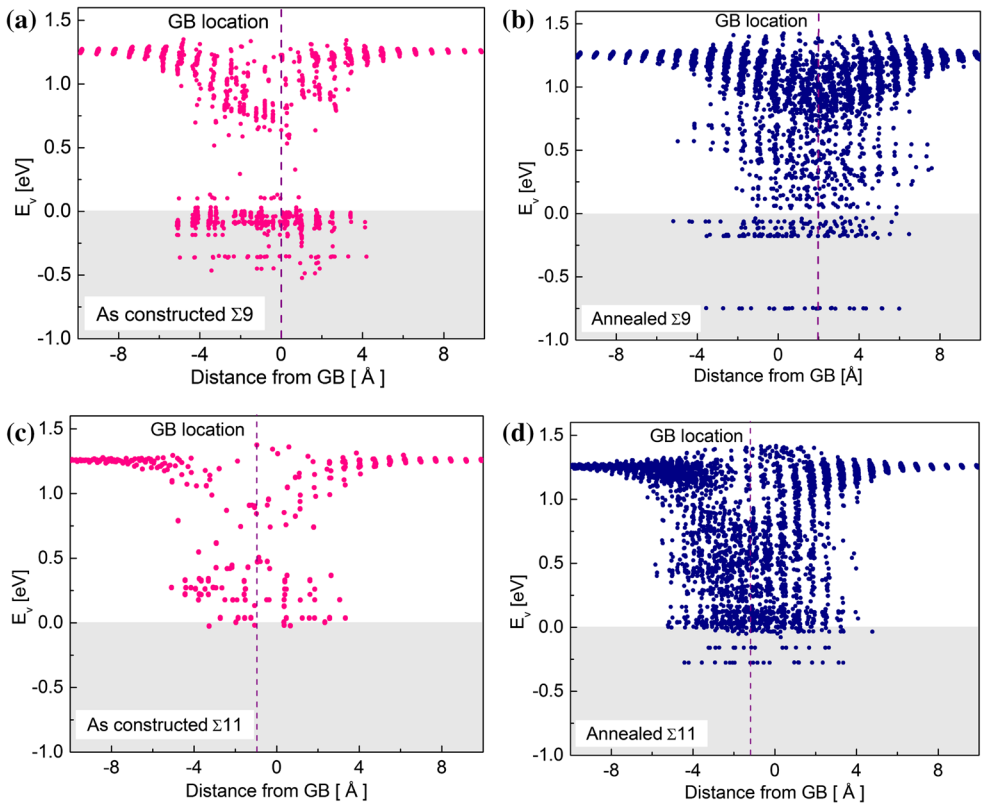

Fig. 5 Vacancy formation energies as a function of distance normal to the GB plane for the **a** as-constructed Σ9 GB, **b** the annealed Σ9 GB, **c** the as-constructed Σ11 GB, and **d** the annealed Σ11 GB

$\sim$0.04 eV for Σ11, and $\sim$0.93 eV for Σ3. Near the maximum energy GB states, the minimum vacancy formation energy is approximately 0 eV for all GBs. States with negative minimum vacancy formation energies occur in all three GBs during vacancy loading.

Because in our vacancy loading algorithm successive GB structures are generated by creating vacancies at the lowest vacancy formation energy site, the minimum GB vacancy formation energy and the GB energy satisfy the following relation:

$$E_v^{\min} = [\gamma_{\mathrm{GB}}(n+1) - \gamma_{\mathrm{GB}}(n)]A_{\mathrm{GB}} \approx \frac{\mathrm{d}\gamma_{\mathrm{GB}}}{\mathrm{d}n}A_{\mathrm{GB}} \qquad (4)$$

Therefore, the cusp in $\gamma_{\mathrm{GB}}(n)$ that occurs near all minimum energy states in all three GBs is simply the consequence of the fact that every such state has a characteristic, non-zero minimum vacancy formation energy.

Structures of minimum energy GB states

In addition to investigating the distribution of vacancy formation energies as a function of position normal to the GB plane, we also examine the vacancy formation energy distribution within the GB plane. To this end, we subdivide GB atoms into groups with high, low, and intermediate vacancy formation energies, as shown in Fig. 6. We then visualize atom distributions in each GB plane by assigning different sizes and colors to atoms in each group. Figures 8, 9, and 10 show the resulting visualizations for the first minimum energy state of Σ9, Σ11, and Σ3, respectively.

Figure 8 shows the structure of the Σ9 GB viewed normal to the GB plane (i.e., along the y direction) and along the $[1\bar{2}\bar{2}]$ direction. The GB contains bands of high and low vacancy formation energy, suggesting that this GB consists of two distinct types of facets. Indeed, both of these bands are symmetrical tilt grain boundary (STGB) facets, denoted here as STGB-α and STGB-β. The tilt axis and plane of STGB-α and -β are $[0\bar{1}1](411)$ and $[\bar{2}\bar{2}1](2\bar{1}2)$, respectively. The dihedral angle between the neighboring facet planes is 135° as shown in Fig. 8. Moreover, the $[1\bar{2}\bar{2}]$ direction, which is orthogonal to the facet boundary $[1\bar{2}\bar{2}]$ and GB normal [201], is precisely the tilt axis of the entire Σ9 GB as a whole.

Unlike the Σ9 GB, the Σ11 GB does not exhibit any facets. Nevertheless, Fig. 9 shows that the Σ11 GB does contain quasi-periodic variations in vacancy formation energy in the [732] and $[2\bar{8}5]$ directions. The lowest

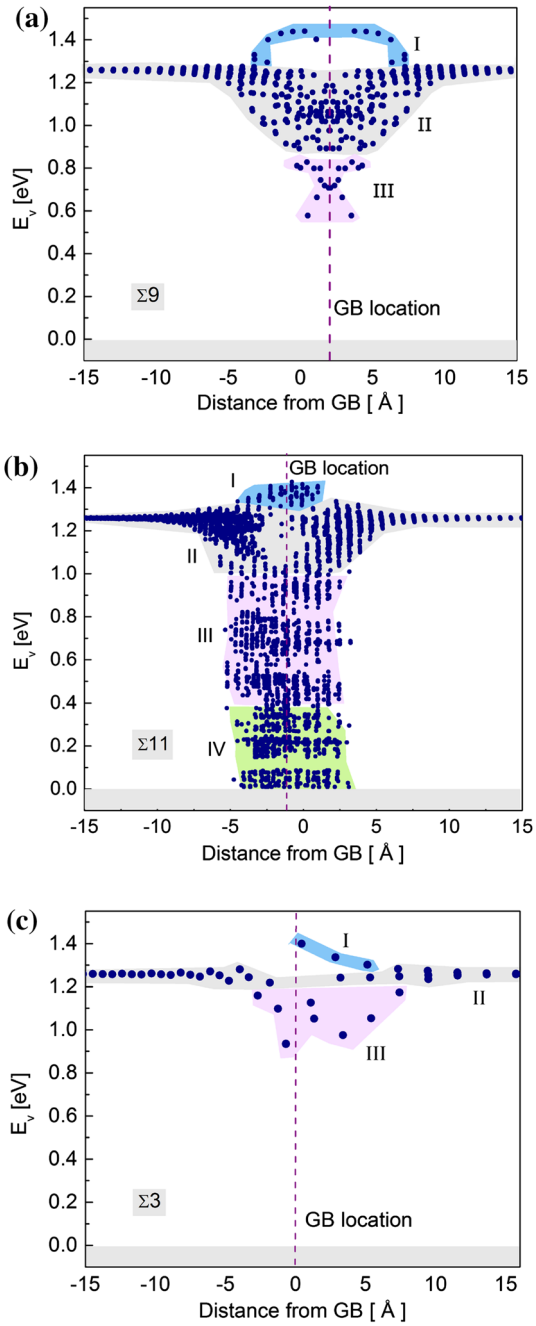

Fig. 6 Vacancy formation energies as a function of distance normal to the GB plane in the first minimum energy state for **a** Σ9 ($n = 49$), **b** Σ11 ($n = 75$), and **c** Σ3 ($n = 0$)

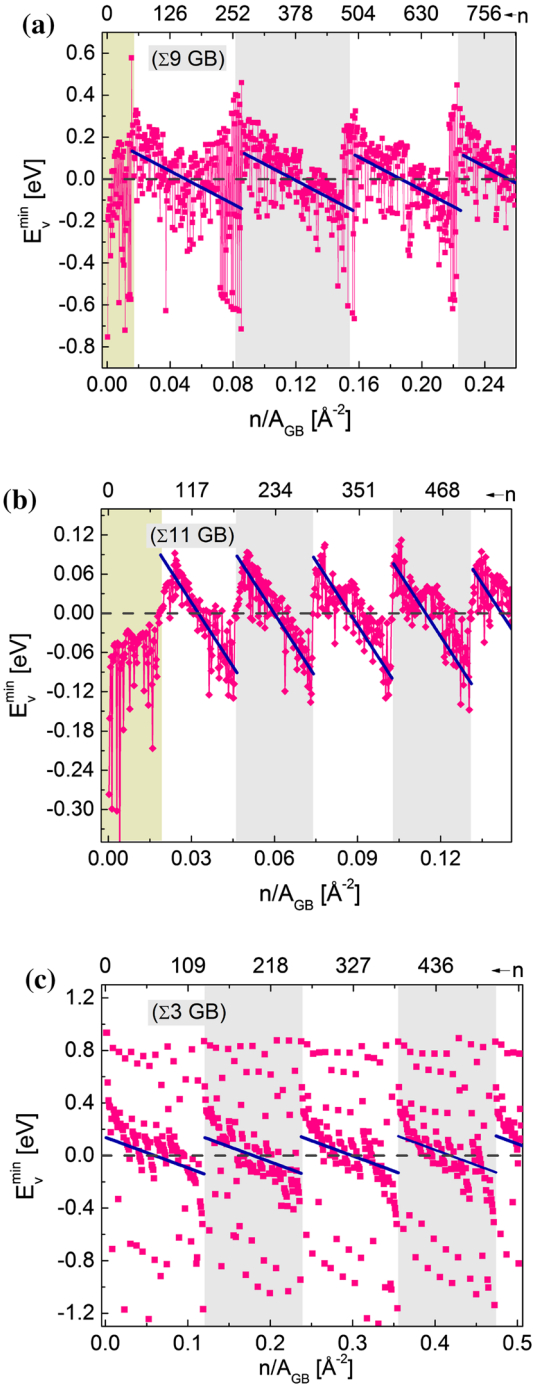

Fig. 7 Minimum GB vacancy formation energies versus n for all three GBs

vacancy formation energy sites (atom type IV in Fig. 9), however, appear not to follow this pattern. Compared with Σ9 and Σ11 GBs, the structure of the Σ3 GB shown in Fig. 10 is relatively simple. It may be described with the structural unit model (SUM) [52] using structural units obtained from the coherent Σ3 twin boundary (CTB) and from the symmetric incoherent Σ3 twin boundary (SITB) [52], denoted in Fig. 10 as 'C' and 'D,' respectively. The former appears like a dumbbell with two connected atoms. The latter is prismatic with four connected atoms. The highest and lowest vacancy formation energies occur at the two vertexes of the 'C' structural unit.

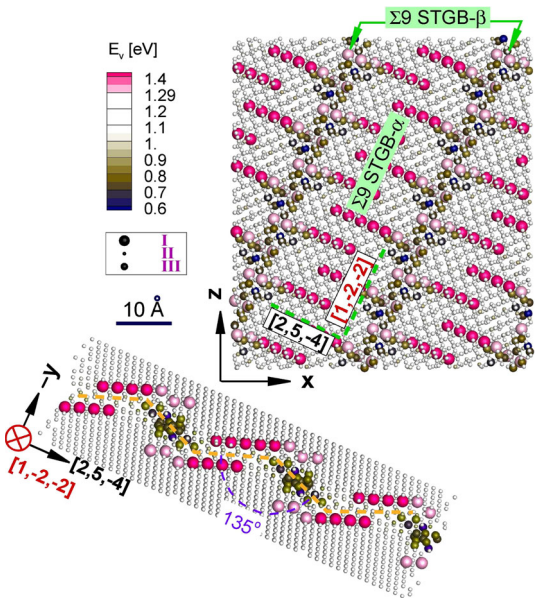

Fig. 8 Structure of the first minimum energy state of the Σ9 GB viewed along the *y* and $[1\bar{2}\bar{2}]$ directions. The view along the $[1\bar{2}\bar{2}]$ direction is tilted so that it constitutes an orthographic projection of the view along the *y* direction. Atoms are sized according to the atom groups shown in Fig. 6a and colored according to vacancy formation energy

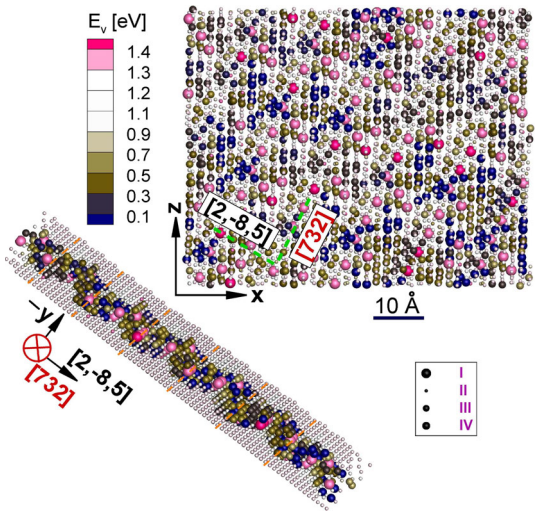

Fig. 9 Structure of the first minimum energy state of the Σ11 GB viewed along the *y* and [732] directions. The view along the [732] direction is tilted so that it constitutes an orthographic projection of the view along the *y* direction. Atoms are sized according to the atom groups shown in Fig. 6b and colored according to vacancy formation energy

Spatial ordering in the vacancy loading sequence

In the algorithm for vacancy loading described in the "Continuous introduction of vacancies into grain boundaries" section, successive GB structures are generated by creating vacancies at sites with lowest vacancy formation energy. We find that consecutive lowest vacancy formation energy sites are not distributed randomly throughout the GBs, but rather exhibit spatial ordering. In some cases, this ordering is correlated to the distribution of location-dependent stresses normal to the GB plane, $\sigma_{yy}(x,z)$, obtained by averaging atomic virial stresses, σ_m^{ij}, contained in a sphere of radius r_{cut} centered on (x,z).

Figure 11 shows contour plots of $\sigma_{yy}(x,z)$, locations where vacancies were loaded (black symbols), and sites with low vacancy formation energies (white symbols) in the Σ9 GB after loading of 21, 41, 61, and 91 vacancies into the first minimum energy GB state (corresponding to $n = 70$, 90, 110, and $n = 140$, respectively). Rather than being distributed uniformly throughout the boundary, all loaded vacancies cluster within the compact region shown by dashed lines. The introduction of vacancies leads to the emergence of tensile stresses ($\sigma_{yy}(x,z) > 0$) in this region. To maintain mechanical equilibrium within the GB, the remainder of the GB develops compressive stresses. Sites with lowest vacancy formation energies occur at the edges of the region shown with dashed lines. Indeed, it appears that the dashed region expanded from its form in Fig. 11a to that in Fig. 11b through vacancies being added along its edges.

In the Σ9 GB, the first complete energy period (see Fig. 2a) involves two stages in the sequence of vacancy loading. During the first half of the period, a region of local tensile stresses such as those shown in Fig. 11 nucleates, grows, and finally covers the entire boundary once ~111 vacancies have been loaded. At this stage, the GB has reached its maximum energy state. Upon further vacancy loading, another tensile region nucleates and grows until it covers the entire boundary, whereupon the GB reaches a new minimum energy state. In the first stage, vacancies are introduced primarily into the STGB-α facet shown in Fig. 8, while in the second stage, most of the vacancies are created in the STGB-β facet. All further energy periods for the Σ9 GB exhibit only one stage of vacancy loading, consisting of the nucleation and growth of a single tensile region. These differences in the vacancy loading stages may account for why the Σ9 GB shears without migrating during the first periodicity and migrates without shearing in the subsequent ones, as detailed in the "Grain boundary migration and shearing" section.

Figure 12 shows snapshots of the Σ11 GB with 35 ($n = 110$) and 85 ($n = 160$) vacancies added to the first minimum energy GB state. As in the Σ9 GB, vacancy insertion sites are not distributed randomly in the GB plane. Vacancies appear to be created preferentially in the bottom-right and top-left regions in the two snapshots shown in Fig. 12. However, they do not cluster into a single

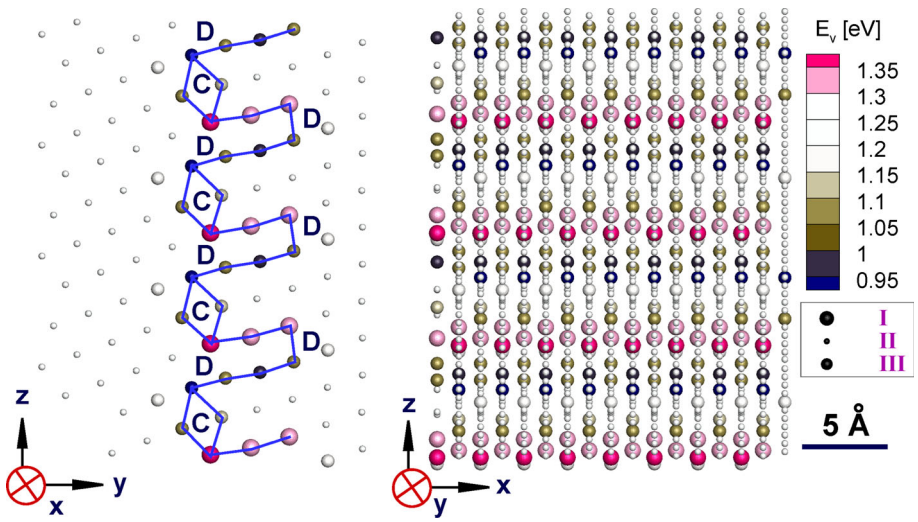

Fig. 10 Structure of the first minimum energy state of the Σ3 GB viewed along the *x* and *y* directions. Atoms are sized according to the atom groups shown in Fig. 6c and colored according to vacancy formation energy. Structural units 'C' and 'D' are taken from the Σ3 CTB and the Σ3 SITB, respectively [52]

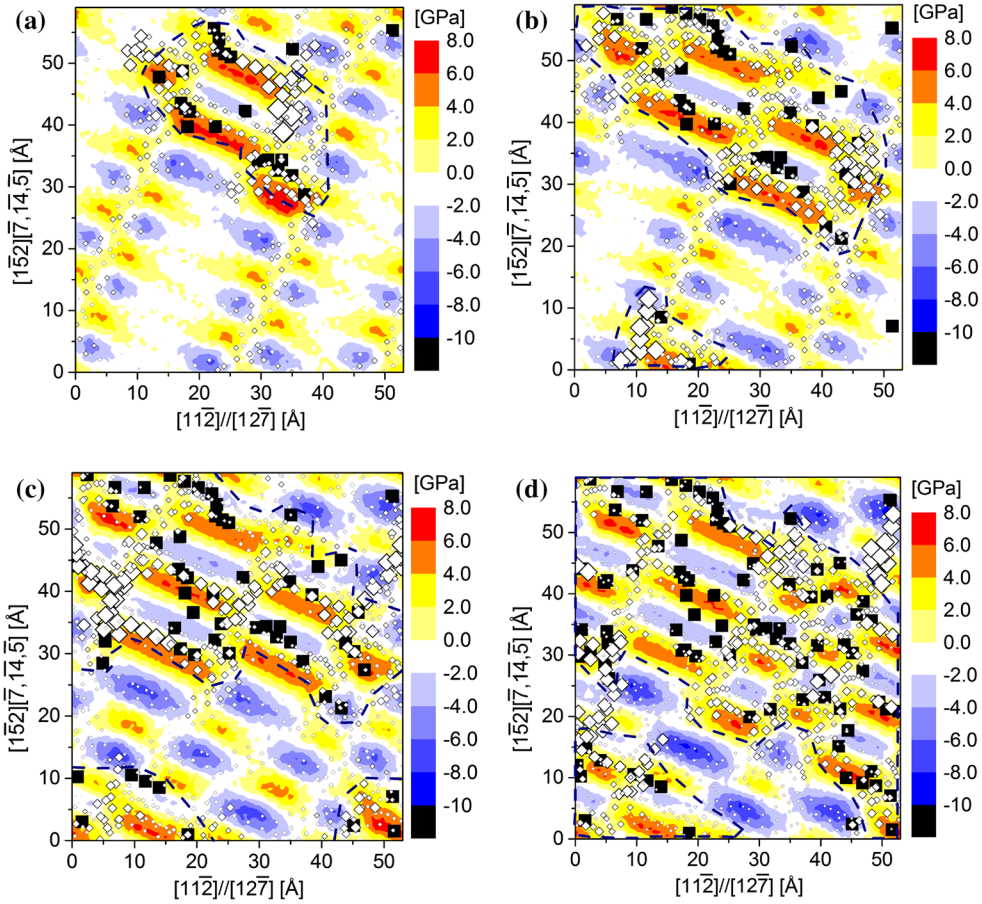

Fig. 11 Contour *plots* of the location-dependent stress normal to the GB plane $\sigma_{yy}(x, z)$ in the Σ9 GB with **a** 21 ($n = 70$), **b** 41 ($n = 90$), **c** 61 ($n = 110$), and **d** 91 ($n = 140$) vacancies introduced into the first minimum energy GB state. *Black-filled* symbols represent sites at which vacancies were created. *Open symbols* represent sites with low vacancy formation energies (the larger the open symbol, the lower the vacancy formation energy)

compact region of tensile stress, as was seen in the Σ9 GB. Furthermore, the Σ11 GB structure itself does not change markedly upon continued vacancy loading. Instead, the initial quasi-periodic GB pattern displaces in the [2$\bar{8}\bar{5}$] direction, as may be seen by comparing the stress fields marked by the dashes squares in Fig. 12a and b.

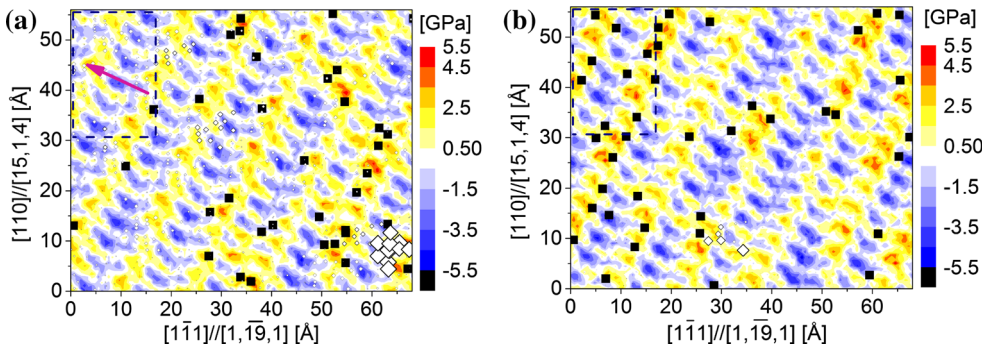

Fig. 12 Contour *plots* of the location-dependent stress normal to the GB plane $\sigma_{yy}(x,z)$ in the Σ11 GB with **a** 35 ($n = 110$) and **b** 85 ($n = 160$) vacancies introduced into the first minimum energy GB state. *Black-filled* symbols represent sites at which vacancies were created. *Open symbols* represent sites with low vacancy formation energies (the larger the *open symbol*, the *lower* the vacancy formation energy)

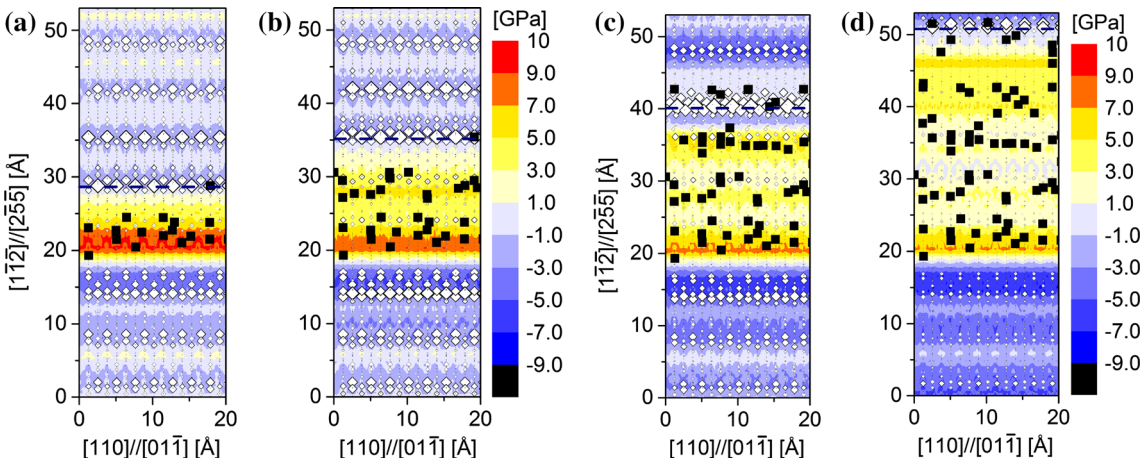

Fig. 13 Contour *plots* of the location-dependent stress normal to the GB plane $\sigma_{yy}(x,z)$ in the Σ3 GB with **a** 18 ($n = 18$), **b** 34 ($n = 34$), **c** 58 ($n = 58$), and **d** 74 ($n = 74$) vacancies introduced into the first minimum energy GB state. *Black-filled* symbols represent sites at which vacancies were created. *Open symbols* represent sites with low vacancy formation energies (the larger the *open symbol*, the *lower* the vacancy formation energy)

Figure 13 shows snapshots of the Σ3 GB with 18($n = 18$), 34 ($n = 34$), 58($n = 58$), and 74 ($n = 74$) vacancies introduced into the first minimum energy GB state. In this boundary, successive vacancies are introduced into adjacent atom rows along the tilt axis (*x*-direction). When nearly all the atoms in a given row have been removed, subsequent vacancies are created in a neighboring atom row. The rest of the atoms in the former row are eventually removed through vacancy-atom exchanges with the latter row. As in the Σ9 GB, a tensile stress develops in the region where vacancies have been removed from the Σ3 GB. To maintain mechanical equilibrium, the GB region where vacancies have not been introduced goes into compression during the vacancy loading process. The boundary between tension and compression is sharper in the Σ3 GB than in the Σ9 GB due to the more regular spatial ordering of removed vacancies in the former.

As in the case of the Σ9 GB, the pattern of vacancy aggregation in the first energy period of the Σ3 GB is different than the pattern in subsequent periods. The as-constructed Σ3 GB has a flat GB plane. During the first energy period, the GB develops a faceted structure, dominated by a large symmetric incoherent twin boundary facet. This faceted structure persists throughout the remaining vacancy loading stages. In all energy periods, vacancies are removed from successive rows along the GB tilt axis, as discussed above. However, in the first period, the succession of rows proceeds in the positive *z*-direction shown in Fig. 13, while in all subsequent periods, the succession is in the negative *z*-direction. These differences in the vacancy loading process may account for why the Σ3 GB migrates without shearing during the first periodicity and shears without migrating in the subsequent ones, as detailed in the "Grain boundary migration and shearing" section.

Discussion

In polycrystalline solids, GBs are likely to reach minimum energy states when allowed to relax for sufficiently long times under thermal equilibrium conditions. Therefore, the minimum energy GBs that we find approximate the likely configuration of thermal equilibrium GBs at low homologous temperatures. At high homologous temperatures, GB entropy may play an important role in determining the thermal equilibrium structures of GBs, which may differ from those found at low temperature [82, 83]. These structures would nevertheless minimize GB free energy. By contrast, the higher energy GB states that we found upon continued vacancy loading represent non-equilibrium GB structures that may form when high vacancy supersaturations are generated, e.g., under irradiation [84].

It is generally accepted that atomistic models of low-energy GB structures usually cannot be obtained by simply joining two grains. Construction of GBs in γ-surface minima and relaxation through high-temperature MD anneals has become standard procedure in atomistic modeling of GBs [73, 85, 86]. More sophisticated methods, such as that of Tschopp et al. and variants of it [52, 61, 62], are also in use. For some specific GBs, such as the $\Sigma3$ and $\Sigma11$ GBs in the present study, these approaches are sufficient to find lowest energy GB states. However, they are not sufficient in all cases, e.g., the $\Sigma9$ GB investigated here. The need to adjust the number of atoms to obtain a low-energy GB model has also been shown previously in modeling of GBs in Si [30] and heterophase interfaces [43].

There is currently no criterion available for determining in advance which GBs require atom addition or removal to reach minimum energy states. Thus, it seems that all GB models must be separately investigated to ascertain if their energies may be lowered this way. A simple first test might be to compute all the vacancy and interstitial formation energies at the GB. In a minimum energy GB, there cannot be any negative point defect energies. It may therefore be expected that studies that did not minimize GB energy with respect to number of atoms may have inadvertently generated high-energy GBs [32, 62]. However, in some cases, the lowest energy GB structures might not be the ones of interest, e.g., when investigating far from equilibrium states [35, 87, 88]. Sometimes, the atomic-level state of a GB might not even be relevant, e.g., for determining the distribution of intrinsic defects [89, 90].

Our study shows how GBs pass between high and low energy states under a continuous influx of vacancies, such as may be expected under irradiation. It also yields insights into how the energies, structures, and properties of such non-equilibrium GBs may differ from those of GBs whose energies have been minimized with respect to the number of atoms present in them.

In our simulations, GB energies vary periodically under continuous vacancy loading. This periodic variation of GB energies arises from the successive removal of atomic planes from the GB. It is consistent with GBs being unsaturable sinks for vacancies. Previous studies have further claimed that most GBs are perfect sinks because their minimum vacancy formation energies are often close to zero or even negative [21, 22, 62]. However, we have shown that as a GB absorbs vacancies, its minimum vacancy formation energies change, starting from positive values near a minimum energy GB state, reaching zero at the maximum energy state, and decreasing to negative values as the next energy minimum is approached.

Therefore, GB sink efficiencies likely depend on the state of the boundary and may vary during the course of vacancy absorption. Because it has positive minimum vacancy formation energy, a minimum energy GB is likely to be a weaker vacancy sink than a higher energy GB. For example, minimum vacancy formation energies at minimum energy $\Sigma9$ and $\Sigma11$ GBs are $\sim$0.46 and $\sim$0.04 eV, respectively, even though the as-constructed and as-annealed versions of these boundaries contain sites with negative vacancy formation energies. In the lowest energy $\Sigma3$ GB, the minimum vacancy formation energy is $\sim$0.93 eV, closer to the vacancy formation energy in fcc Cu (1.27 eV, for the potential used here). However, high-energy $\Sigma3$ GBs contain negative vacancy formation energy sites, as well.

We observe that minimum vacancy formation energies in the minimum energy states of all three GBs investigated here correlate well with the void denuded zone widths of the same GBs measured under irradiation in Ref. [5], as shown in Fig. 14. This finding suggests that GBs in an irradiated material are likely near equilibrium throughout the irradiation process, even as they absorb vacancies from

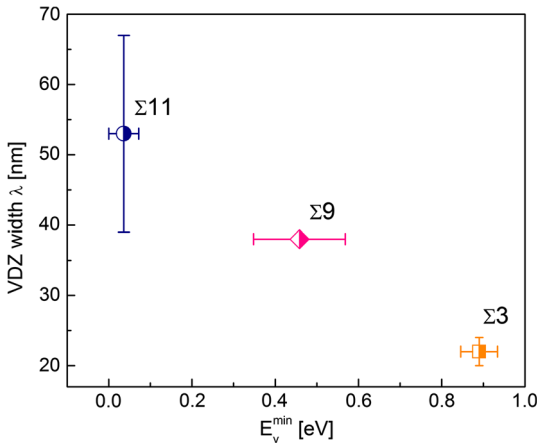

Fig. 14 Void denuded zone widths from Ref. [5] (see Table 1) plotted against minimum vacancy formation energies in the lowest energy states for the GBs investigated here

the adjacent crystalline material. For example, the more efficient re-emission of vacancies from equilibrium GBs may prolong the time that the GB spends near equilibrium. By contrast, when a GB markedly departs from its equilibrium state, it may become a much better vacancy sink, re-emitting vacancies at a lower rate, and therefore rapidly accumulating the additional vacancies it needs to arrive at the next equilibrium state.

Additional insight into the sink action of GBs under irradiation may be gained from our investigation of spatial ordering in the sequence of vacancy loading into GBs ("Spatial ordering in the vacancy loading sequence" section). In the Σ9 and Σ3 GBs, locations of lowest vacancy formation energy tend to concentrate at the edge of the region where vacancies were previously introduced. This edge may be thought of as a one-dimensional extrinsic "defect" that is a preferential site for vacancy absorption. The GB area enclosed by this defect increases as more vacancies are added.

Similar observations were made by King and Smith in their transmission electron microscopy (TEM) study on point defect absorption by GBs under electron irradiation [3]. They showed that point defect absorption at GBs was accompanied by the climb (or climb-plus-glide) of GB dislocations and by the formation and growth of triangular dislocation loops on a coherent twin boundary (CTB). Based on these findings, they concluded that GBs accommodate a continuous influx of vacancies through dislocation mechanisms [91]. Yu et al. later showed that extended defects, such as stacking fault tetrahedra (SFT), may also be absorbed by GBs through such mechanisms [92].

Following King and Smith, we propose that the one-dimensional "defect" where preferential vacancy trapping occurs in our simulations may be thought of as the core of a dislocation. This hypothesis is consistent with the emergence of tensile stresses in the region enclosed by this defect, suggesting that the defect may be thought of as a generalized vacancy dislocation loop. However, the vacancy loops in our simulations are more difficult to visualize than dislocations in the CTBs studied by King and Smith because the internal structure of the non-coherent GBs investigated here is considerably more complex than that of CTBs.

According to the interpretation proposed above, vacancies loaded into a GB initially in a minimum energy state agglomerate to nucleate a small vacancy loop. The loop expands as further vacancies are loaded. However, only the core of the loop contains low vacancy formation energy sites. The area inside and outside the loop closely resembles the structure of the GB in its minimum energy state, with correspondingly higher vacancy formation energies. Indeed, the lower minimum vacancy formation energy in the minimum energy state of the Σ11 GB may be partially responsible for the more uniform absorption of vacancies across the area of this boundary, compared to the Σ9 and Σ3 GBs. Absorption of vacancies into the cores of expanding vacancy loops provides additional insight into how GBs may simultaneously be unsaturable vacancy sinks and yet remain near thermal equilibrium: vacancies may be continuously absorbed by trapping at cores of nucleating and expanding loops, while most vacancy formation energies in the majority of the GB area remain near their thermal equilibrium values.

The periodic variations in GB energy when $n > 49$ and $n > 0$ for Σ9 and Σ3 GBs shown in Fig. 2a and c may be attributed to changes in the line length of GB vacancy loops. The baseline energy for all GB structures—including those far from equilibrium—is then the energy of the GB in its minimum energy state. As a vacancy loop nucleates and grows, its line length increases, giving rise to the increase in energy as a function of vacancy loading shown in Fig. 2a and c. This loop expands as further vacancies are added. Once it has grown to a size comparable to the dimensions of the simulation cell, it reacts with its periodic images, coalescing with them and forming a loop that shrinks as vacancies are added, as illustrated in Fig. 15. This latter loop may be thought of as an interstitial loop in the next minimum energy state of the GB into which vacancies are being loaded.

This process of vacancy absorption is analogous to island growth and coalescence in physical vapor deposition

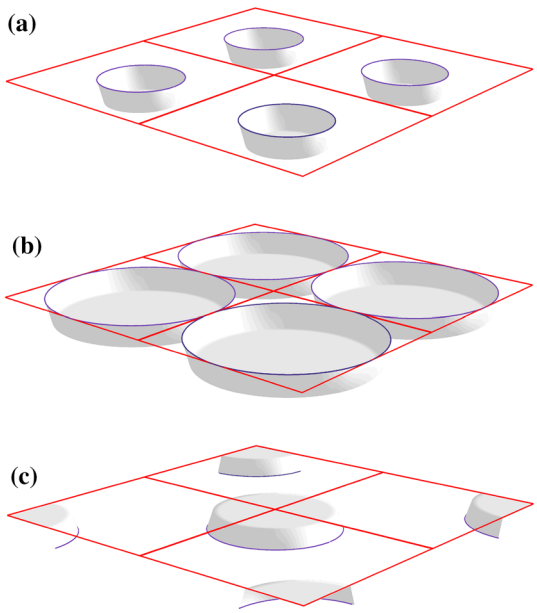

Fig. 15 Growth of GB vacancy loops in four periodic images of the simulation cell: **a** nucleation of vacancy loops, **b** growth of vacancy loops and impingement of their periodic images upon each other, and **c** reaction of periodic images into interstitial-like loops that shrink upon further vacancy loading

on crystal surfaces [93]. The sink efficiency of the GB is determined by the rate of re-emission of vacancies from the near-equilibrium GB regions. This rate would also depend on the diffusivity of vacancies within the GB, which would determine the likelihood of re-emission prior to absorption at the core of an expanding vacancy loop [84].

The introduction of vacancies also changes a GB's specific excess volume and GB stress. Several investigators have argued for a monotonic relation between GB energy and excess volume [66, 74–81]. Our study adds an important qualification to this view by showing that it applies only to comparisons between different GBs in their minimum energy states, not to comparisons between different states of the same GB or between different GBs driven far from equilibrium. In view of the discussion above, it may be hypothesized that these changes in volume are due to the vacancy loops that nucleate and grow at GBs during continuous vacancy loading. Linear elasticity theory predicts that dislocation elastic fields are dilatation-free [91], so these changes in volume would have to be due to the detailed core structure of these dislocations.

We also find that GB stresses increase monotonically with specific excess volume. This finding may play a role in explaining changes in GB stresses that occur during annealing of nanocrystalline metals [70]. The elastic fields of GB vacancy loops may be useful in modeling variations in GB stresses. Finally, the excess volume of the $\Sigma 11$ GB varies periodically with vacancy loading, yet there are no such clear trends for other two GBs. These observations identify attractive topics for follow-on investigations.

Previous experimental studies have observed migration of $\Sigma 3$ coherent and symmetric incoherent twin boundaries under continuous radiation-induced point defect fluxes [94–98]. We show that continuous absorption of vacancies may also cause GBs to shear. Because our simulations are performed under periodic boundary conditions, adjacent grains in our models may displace parallel to the GB plane without producing compatibility stresses. However, in real polycrystalline solids, GBs cannot shear freely due to confinement by other neighboring grains. Thus, rather than giving rise to unconstrained GB shearing, vacancy fluxes into GBs in irradiated polycrystalline solids may instead lead to the buildup of internal compatibility stresses. These stresses may in turn influence radiation-induced microstructure evolution.

Conclusions

We have conducted an atomistic modeling study of continuous vacancy loading into three non-coherent GBs in Cu using a quasi-static algorithm where successive vacancies are introduced into the lowest vacancy formation energy site at the boundary. Our main conclusions are

1. Building an atomistic model of a GB in its minimum energy state requires adjusting the number of atoms in the GB.
2. GB energies vary periodically with the number of vacancies absorbed. The recurrence of lowest energy GB states during vacancy influx indicates that GBs are unsaturable sinks for vacancies.
3. GB energies and specific excess volumes are proportional to each other for different GBs in their minimum energy states. However, there is no proportionality between the energies and specific excess volumes of non-equilibrium states of individual GBs.
4. GB stresses increase monotonically with specific excess volumes for all three GBs studied.
5. Continuous vacancy influx causes GBs to migrate and to shear.
6. The void denuded zone widths measured in Ref. [5] for the three GBs modeled here are proportional to the minimum vacancy formation energies of these boundaries in their lowest energy states.
7. In two of the three GBs modeled here, successive vacancies introduced into the boundary appear to accumulate at the core of a generalized vacancy dislocation loop. The sink action of GBs may be due to vacancy absorption at such extrinsic dislocation loops, while GB sink efficiency is determined by vacancy re-emission from the GB area inside and outside these loops.

Acknowledgements MJD thanks A. P. Sutton and R. Birringer for useful discussions. This work was supported by the Center for Materials at Irradiation and Mechanical Extremes, an Energy Frontier Research Center funded by the U.S. Department of Energy, Office of Science, Office of Basic Energy Sciences under Award Number 2008LANL1026.

References

1. Dollar M, Gleiter H (1985) Point-defect annihilation at grain-boundaries in gold. Scripta Metall 19(4):481–484
2. Gleiter H (1979) Grain-boundaries as point-defect sources or sinks - diffusional creep. Acta Metall Mater 27(2):187–192
3. King AH, Smith DA (1980) On the mechanisms of point-defect absorption by grain and twin boundaries. Philos Mag A 42(4):495–512
4. Siegel RW, Chang SM, Balluffi RW (1980) Vacancy loss at grain-boundaries in quenched polycrystalline gold. Acta Metall Mater 28(3):249–257
5. Han WZ, Demkowicz MJ, Fu EG, Wang YQ, Misra A (2012) Effect of grain boundary character on sink efficiency. Acta Mater 60(18):6341–6351
6. Misra A, Demkowicz MJ, Zhang X, Hoagland RG (2007) The radiation damage tolerance of ultra-high strength nanolayered composites. Jom-Us 59(9):62–65
7. Misra A, Thilly L (2010) Structural metals at extremes. MRS Bull 35(12):965–976

8. Han WZ, Demkowicz MJ, Mara NA, Fu EG, Sinha S, Rollett AD, Wang YQ, Carpenter JS, Beyerlein IJ, Misra A (2013) Design of radiation tolerant materials via interface engineering. Adv Mater 25(48):6975–6979
9. Demkowicz MJ, Hoagland RG, Uberuaga BP, Misra A (2011) Influence of interface sink strength on the reduction of radiation-induced defect concentrations and fluxes in materials with large interface area per unit volume. Phys Rev B 84(10):104102
10. King AH, Smith DA (1981) Calculations of sink strength and bias for point-defect absorption by dislocations in arrays. Radiat Eff Defect Solids 54(3–4):169–176
11. Millett PC, Aidhy DS, Desai T, Phillpot SR, Wolf D (2009) Grain-boundary source/sink behavior for point defects: an atomistic simulation study. Int J Mater Res 100(4):550–555
12. Zhang YF, Huang HC, Millett PC, Tonks M, Wolf D, Phillpot SR (2012) Atomistic study of grain boundary sink strength under prolonged electron irradiation. J Nucl Mater 422(1–3):69–76
13. Singh BN (1974) Effect of grain-size on void formation during high-energy electron-irradiation of austenitic stainless-steel. Philos Mag 29(1):25–42
14. Ashby MF (1969) On interface-reaction control of nabarro-herring creep and sintering. Scripta Metall 3(11):837–842
15. Sutton AP, Balluffi RW (1995) Interfaces in crystalline materials. Clarendon Press, Oxford
16. Bristowe PD, Brokman A, Spaepen F, Balluffi RW (1980) Simulation of the structure of vacancies in high angle grain-boundaries. Scripta Metall 14(8):943–950
17. Brokman A, Bristowe PD, Balluffi RW (1981) Computer-simulation study of the structure of vacancies in grain-boundaries. J Appl Phys 52(10):6116–6127
18. Chen D, Wang J, Chen TY, Shao L (2013) Defect annihilation at grain boundaries in alpha-Fe. Sci Rep 3:1450
19. Demkowicz MJ, Anderoglu O, Zhang XH, Misra A (2011) The influence of Sigma 3 twin boundaries on the formation of radiation-induced defect clusters in nanotwinned Cu. J Mater Res 26(14):1666–1675
20. Rhodes NR, Tschopp MA, Solanki KN (2013) Quantifying the energetics and length scales of carbon segregation to alpha-Fe symmetric tilt grain boundaries using atomistic simulations. Model Simul Mater Sci 21(3):035009
21. Suzuki A, Mishin Y (2003) Interaction of point defects with grain boundaries in fcc metals. Interface Sci 11(4):425–437
22. Suzuki A, Mishin Y (2003) Atomistic modeling of point defects and diffusion in copper grain boundaries. Interface Sci 11(1):131–148
23. Sorensen MR, Mishin Y, Voter AF (2000) Diffusion mechanisms in Cu grain boundaries. Phys Rev B 62(6):3658–3673
24. Hahn W, Gleiter H (1981) On the structure of vacancies in grain-boundaries. Acta Metall Mater 29(4):601–606
25. Uberuaga BP, Bai XM, Dholabhai PP, Moore N, Duffy DM (2013) Point defect-grain boundary interactions in MgO: an atomistic study. J Phys Condens Matter 25(35):355001
26. Vitek V, Sutton AP, Gui Jin W, Schwartz D (1983) On the multiplicity of structures and grain boundaries. Scripta Metall 17(2):183–189
27. Vitek V, Minonishi Y, Wang G-J (1985) Multiplicity of grain boundary structures : vacancies in boundaries and transformations of the boundary structure. J Phys Colloques 46(C4):C4-171
28. Phillpot SR, Rickman JM (1992) Simulated quenching to the zero-temperature limit of the grand-canonical ensemble. J Chem Phys 97(4):2651–2658
29. Phillpot SR, Rickman JM (1992) Reconstruction of a high-angle twist grain-boundary by grand-canonical simulated quenching. Struct Prop Interfaces Mater 238:183–188
30. von Alfthan S, Haynes PD, Kaski K, Sutton AP (2006) Are the structures of twist grain boundaries in silicon ordered at 0 K? Phys Rev Lett 96(5):055505
31. Bai XM, Voter AF, Hoagland RG, Nastasi M, Uberuaga BP (2010) Efficient annealing of radiation damage near grain boundaries via interstitial emission. Science 327(5973):1631–1634
32. Bai XM, Vernon LJ, Hoagland RG, Voter AF, Nastasi M, Uberuaga BP (2012) Role of atomic structure on grain boundary-defect interactions in Cu. Phys Rev B 85(21):204103
33. Frolov T, Olmsted DL, Asta M, Mishin Y (2013) Structural phase transformations in metallic grain boundaries. Nat Commun 4:1899
34. Borovikov V, Tang XZ, Perez D, Bai XM, Uberuaga BP, Voter AF (2013) Influence of point defects on grain boundary mobility in bcc tungsten. J Phys Condens Matter 25(3):035402
35. Tucker GJ, McDowell DL (2011) Non-equilibrium grain boundary structure and inelastic deformation using atomistic simulations. Int J Plast 27(6):841–857
36. Kolluri K, Demkowicz MJ (2010) Dislocation mechanism of interface point defect migration. Phys Rev B 82(19):193404
37. Kolluri K, Demkowicz MJ (2012) Formation, migration, and clustering of delocalized vacancies and interstitials at a solid-state semicoherent interface. Phys Rev B 85(20):205416
38. Kolluri K, Demkowicz MJ, Hoagland RG, Liu XY (2013) Behavior of vacancies and interstitials at semicoherent interfaces. Jom-Us 65(3):374–381
39. Martínez E, Hirth JP, Nastasi M, Caro A (2012) Structure of a 2 degree (010) Cu twist boundary interface and the segregation of vacancies and He atoms. Phys Rev B 85(6):060101
40. Martínez E, Caro A (2012) Atomistic modeling of long-term evolution of twist boundaries under vacancy supersaturation. Phys Rev B 86(21):214109
41. Gavini V, Bhattacharya K, Ortiz M (2007) Vacancy clustering and prismatic dislocation loop formation in aluminum. Phys Rev B 76(18):180101
42. Sabochick MJ, Yip S, Lam NQ (1988) Atomistic simulation study of large vacancy clusters in copper. J Phys F 18(3):349
43. Demkowicz MJ, Hoagland RG, Hirth JP (2008) Interface structure and radiation damage resistance in Cu–Nb multilayer nanocomposites. Phys Rev Lett 100(13):136102
44. Cantwell PR, Tang M, Dillon SJ, Luo J, Rohrer GS, Harmer MP (2014) Grain boundary complexions. Acta Mater 62:1–48
45. Hasnaoui A, Van Swygenhoven H, Derlet PM (2002) On non-equilibrium grain boundaries and their effect on thermal and mechanical behaviour: a molecular dynamics computer simulation. Acta Mater 50(15):3927–3939
46. Kempshall BW, Prenitzer BI, Giannuzzi LA (2002) Grain boundary segregation: equilibrium and non-equilibrium conditions. Scripta Mater 47(7):447–451
47. Pumphrey PH, Gleiter H (1975) Structure of nonequilibrium high-angle grain-boundaries. Philos Mag 32(4):881–885
48. Randle V (1993) The measurement of grain boundary geometry. Institute of Physiscs Publishing, Bristol
49. Grimmer H (1976) Coincidence-site lattices. Acta Crystallogr A 32(5):783–785
50. Randle V (1998) Overview no. 127. The role of the grain boundary plane in cubic polycrystals. Acta Mater 46(5):1459–1480
51. Bollmann W (1970) Crystal defects and crystalline interfaces. Springer, Berlin
52. Tschopp MA, McDowell DL (2007) Structures and energies of Sigma 3 asymmetric tilt grain boundaries in copper and aluminium. Philos Mag 87(22):3147–3173
53. Daw MS, Baskes MI (1984) Embedded-atom method—derivation and application to impurities, surfaces, and other defects in metals. Phys Rev B 29(12):6443–6453
54. Mishin Y, Mehl MJ, Papaconstantopoulos DA, Voter AF, Kress JD (2001) Structural stability and lattice defects in copper: Ab initio, tight-binding, and embedded-atom calculations. Phys Rev B 63(22):224106

55. Bertsekas D (1999) Nonlinear programming. Athena Scientific, Belmont
56. Hoover WG (1985) Canonical dynamics—equilibrium phase-space distributions. Phys Rev A 31(3):1695–1697
57. Nose S (1984) A unified formulation of the constant temperature molecular-dynamics methods. J Chem Phys 81(1):511–519
58. Plimpton S (1995) Fast parallel algorithms for short-range molecular dynamics. J Comp Phys 117(1):1–19
59. Alexander S (2010) Visualization and analysis of atomistic simulation data with OVITO–the open visualization tool. Model Simul Mater Sci 18(1):015012
60. Daw MS, Foiles SM, Baskes MI (1993) The embedded-atom method: a review of theory and applications. Mater Sci Rep 9(7–8):251–310
61. Tschopp MA, McDowell DL (2007) Asymmetric tilt grain boundary structure and energy in copper and aluminium. Philos Mag 87(25):3871–3892
62. Tschopp MA, Solanki KN, Gao F, Sun X, Khaleel MA, Horstemeyer MF (2012) Probing grain boundary sink strength at the nanoscale: energetics and length scales of vacancy and interstitial absorption by grain boundaries in alpha-Fe. Phys Rev B 85(6):064108
63. Fensin SJ, Valone SM, Cerreta EK, Gray GT (2012) Influence of grain boundary properties on spall strength: grain boundary energy and excess volume. J Appl Phys 112(8):083529
64. Brown JA, Mishin Y (2007) Dissociation and faceting of asymmetrical tilt grain boundaries: molecular dynamics simulations of copper. Phys Rev B 76(13):134118
65. Rycroft CH, Grest GS, Landry JW, Bazant MZ (2006) Analysis of granular flow in a pebble-bed nuclear reactor. Phys Rev E 74(2):021306
66. Wolf D (1989) Correlation between energy and volume expansion for grain-boundaries in fcc metals. Scripta Metall 23(11):1913–1918
67. Cammarata RC (1994) Surface and interface stress effects in thin films. Prog Surf Sci 46(1):1–38
68. Spaepen F (2000) Interfaces and stresses in thin films. Acta Mater 48(1):31–42
69. Du D, Zhang H, Srolovitz DJ (2007) Properties and determination of the interface stiffness. Acta Mater 55(2):467–471
70. Birringer R, Zimmer P (2009) Grain- and phase-boundary stress effects in nanocrystalline materials. Acta Mater 57(6):1703–1716
71. Shull AL, Spaepen F (1996) Measurements of stress during vapor deposition of copper and silver thin films and multilayers. J Appl Phys 80(11):6243–6256
72. Kelchner CL, Plimpton SJ, Hamilton JC (1998) Dislocation nucleation and defect structure during surface indentation. Phys Rev B 58(17):11085–11088
73. Cahn JW, Mishin Y, Suzuki A (2006) Coupling grain boundary motion to shear deformation. Acta Mater 54(19):4953–4975
74. Seeger A, Schottky G (1959) Energy and electrical resistivity of high-angle grain boundaries in metals. Acta Metall Mater 7(7):495–503
75. Wolf D (1989) Structure-energy correlation for grain-boundaries in fcc metals.2. Boundaries on the (110) and (113) planes. Acta Metall Mater 37(10):2823–2833
76. Wolf D (1989) Structure-energy correlation for grain-boundaries in fcc metals.1. Boundaries on the (111) and (100) planes. Acta Metall Mater 37(7):1983–1993
77. Wolf D (1990) Structure-energy correlation for grain-boundaries in fcc metals.4. Asymmetrical twist (general) boundaries. Acta Metall Mater 38(5):791–798
78. Wolf D (1990) Structure-energy correlation for grain-boundaries in fcc metals.3. Symmetrical tilt boundaries. Acta Metall Mater 38(5):781–790
79. Wolf D (1990) Correlation between the energy and structure of grain-boundaries in bcc metals.1. Symmetrical boundaries on the (110) and (100) planes. Philos Mag B 59(6):667–680
80. Wolf D (1990) Correlation between the energy and structure of grain-boundaries in bcc metals.2. Symmetrical tilt boundaries. Philos Mag A 62(4):447–464
81. Olmsted DL, Foiles SM, Holm EA (2009) Survey of computed grain boundary properties in face-centered cubic metals: I. Grain boundary energy. Acta Mater 57(13):3694–3703
82. Olmsted DL, Buta D, Adland A, Foiles SM, Asta M, Karma A (2011) Dislocation-pairing transitions in hot grain boundaries. Phys Rev Lett 106(4):046101
83. Olmsted DL, Foiles SM, Holm EA (2007) Grain boundary interface roughening transition and its effect on grain boundary mobility for non-faceting boundaries. Scripta Mater 57(12):1161–1164
84. Was GS (2007) Fundamentals of radiation materials science: metals and alloys. Springer Verlag, Berlin
85. Duesbery MS, Vitek V (1998) Plastic anisotropy in bcc transition metals. Acta Mater 46(5):1481–1492
86. Spearot DE, Tschopp MA, Jacob KI, McDowell DL (2007) Tensile strength of $\langle 100 \rangle$ and $\langle 110 \rangle$ tilt bicrystal copper interfaces. Acta Mater 55(2):705–714
87. Rittner JD, Seidman DN (1996) $\langle 110 \rangle$ symmetric tilt grain-boundary structures in fcc metals with low stacking-fault energies. Phys Rev B 54(10):6999–7015
88. Rupert TJ, Schuh CA (2012) Mechanically driven grain boundary relaxation: a mechanism for cyclic hardening in nanocrystalline Ni. Phil Mag Lett 92(1):20–28
89. Vattre AJ, Demkowicz MJ (2013) Determining the Burgers vectors and elastic strain energies of interface dislocation arrays using anisotropic elasticity theory. Acta Mater 61(14):5172–5187
90. Vattre AJ, Abdolrahim N, Kolluri K, Demkowicz MJ (2014) Computational design of patterned interfaces using reduced order models. Sci Rep 4:6231
91. Hirth JP, Lothe J (1967) Theory of dislocations. McGraw-Hill, New York
92. Takahashi H, Hashimoto N, Kanda H (1996) Effects of excess point defects flow and interface orientation on grain boundary migration under irradiation. Interface Sci 4(3–4):221–228
93. Freund H-J (2002) Clusters and islands on oxides: from catalysis via electronics and magnetism to optics. Surf Sci 500(1–3):271–299
94. Li N, Wang J, Wang YQ, Serruys Y, Nastasi M, Misra A (2013) Incoherent twin boundary migration induced by ion irradiation in Cu. J Appl Phys 113(2):023508
95. Yu KY, Bufford D, Khatkhatay F, Wang H, Kirk MA, Zhang X (2013) In situ studies of irradiation-induced twin boundary migration in nanotwinned Ag. Scripta Mater 69(5):385–388
96. Yu KY, Bufford D, Sun C, Liu Y, Wang H, Kirk MA, Li M, Zhang X (2013) Removal of stacking-fault tetrahedra by twin boundaries in nanotwinned metals. Nat Commun 4:1377
97. Foiles SM, Medlin DL (2001) Structure and climb of 1/3 $\langle 111 \rangle$ twin dislocations in aluminum. Mater Sci Eng 319:102–106
98. Medlin DL, Carter CB, Angelo JE, Mills MJ (1997) Climb and glide of a/3 $\langle 111 \rangle$ dislocations in an aluminium $\sigma = 3$ boundary. Philos Mag A 75(3):733–747